(equation (1)) is modified to a sum over a continuum of instantaneous transport vectors, with the component of gross transport normal to the bedforms given by

$$T = \sum_i D_i |\sin(\gamma_i - \alpha)| \qquad (2)$$

where i ranges over all transport vectors. Although in this more general case of many transport vectors there is no analytical solution for α, the gross, bedform-normal transport T can be maximized numerically to give bedform orientation.

In the bidirectional, rotating table experiments[17], transport vectors **D** and **S** were proportional to the duration of steady winds in each direction, and thus the bedform orientation α depended on the ratio $|\mathbf{D}|/|\mathbf{S}|$ (equation (1)) and not on a particular sediment transport model. However, the more general solution requires a sediment transport model to represent D_i. Similar to bedload models[25], D_i was calculated as proportional to the instantaneous velocity cubed. The results are not sensitive to the exponent of the velocity used to calculate D_i. Here, the individual instantaneous (2 Hz) transport vectors (calculated from velocity measurements) were summed over a 3-h period and sorted into 5°-wide directional bins, giving a directional distribution of cumulative transport (see, for example, Fig. 4b). The distribution was used to calculate T (equation (2)), with γ_i and D_i equal to the direction and corresponding magnitude of the cumulative transport in each bin. The value of α for which T is maximum was then found for each 3-h period. The model is sensitive to the estimation period and better results were obtained with shorter periods, implying that the bedforms respond quickly (order 3 h) to changes in the flow field.

For comparison with megaripple migration direction observations, 16 sequential 3-h estimates of α were averaged to give a 48-h estimate. Assuming that megaripples migrate ~90° to their crest orientation, a predicted migration direction is given by $\theta_{RH} = 90° - \alpha$. As shown in Fig. 3d, θ_{RH} predicts accurately the observed megaripple migration direction θ_{Mrip} (the slope (1.04) of a best-fit line does not differ significantly from 1.00 at the 99.5% level).

These observations suggest that megaripple migration in the surf zone is caused by both mean and wave flows. However, the migration direction is not aligned with the vector sum of the currents, but so that gross sediment transport normal to the bedform is maximized, as suggested previously for subaerial features[17]. Megaripples in the surf zone of a natural barred beach occur frequently for a wide range of wave and current conditions, and include transverse, longitudinal and oblique bedforms. If migration of bedforms is an important mechanism for bedload sediment transport, parametrizations that depend only on waves, currents, or even their vector sum, may not predict the observed transport accurately. Conversely, flow conditions inferred from alignment of bed features preserved in ancient sedimentary deposits or observed in modern environments may not be unique because different flow fields can maximize gross bedform-normal transport. □

Received 29 December 1997; accepted 28 April 1998.

1. Clifton, H. E., Hunter, R. E. & Phillips, R. L. Depositional structures and processes in the non-barred high-energy nearshore. *J. Sedim. Petrol.* **41,** 651–670 (1971).
2. Bagnold, R. A. *The Physics of Wind Blown Sand and Desert Dunes* (Methuen, London, 1954).
3. Simons, D. B. & Richardson, E. V. Forms of bed roughness in alluvial channels. *Am. Soc. Civ. Eng. Trans.* **128,** 284–302 (1963).
4. Dalrymple, R. W., Knight, R. J. & Lambiase, J. J. Bedforms and their hydraulic stability relationships in a tidal environment, Bay of Fundy, Canada. *Nature* **275,** 100–104 (1978).
5. Southard, J. B., Lambie, J. M., Federico, D. C., Pile, H.T. & Weidman, C. R. Experiments on bed configurations in fine sands under bidirectional purely oscillatory flow, and the origin of hummocky cross-stratification. *J. Sedim. Petrol.* **60,** 1–17 (1990).
6. Garcez Faria, A. F., Thornton, E. B., Stanton, T. P., Soares, C. V. & Lippmann, T. C. Vertical profiles of longshore currents and related bed shear stress and bottom roughness. *J. Geophys. Res.* **103,** 3217–3232 (1998).
7. Allen, J. R. L. *Current Ripples: Their Relation to Patterns of Water and Sediment Motion* (North-Holland, Amsterdam, 1968).
8. Middleton, G. V. & Southard, J. B. *Mechanics of Sediment Movement.* (Lecture for short course no. 3, Society of Economic Paleontologists and Mineralogists, 1982).
9. Davidson-Arnott, R. G. D. & Greenwood, B. Facies relationships on a barred coast, Kouchibouguac Bay, New Brunswick, Canada. *Beach and Nearshore Sedimentation, SEPM Special Pub.* **24,** 149–169 (1976).
10. Sherman, D. J. & Greenwood, B. Hummocky cross-stratification and post-vertex ripples: length scales and hydraulic analysis. *Sedimentology* **36,** 981–986 (1989).
11. Werner, B. T. Eolian dunes: computer simulations and attractor interpretation. *Geology* **23,** 1107–1110 (1995).
12. Stam, J. M. T. On the modelling of two-dimensional aeolian dunes. *Sedimentology* **44,** 127–141 (1997).
13. Bagnold, R. A. Journeys in the Libyan Desert 1929 and 1939. *Geogr. J.* **78,** 13–39 (1933).
14. Warren, A. Dune trend and the Ekman spiral. *Nature* **259,** 653–654 (1976).
15. Tsoar, H. Dynamic processes operating on a longitudinal (seif) sand dune. *Sedimentology* **30,** 567–578 (1983).
16. Hanna, S. R. The formation of longitudinal sand dunes by large helical eddies in the atmosphere. *J. Appl. Meteorol.* **8,** 874–883 (1969).
17. Rubin, D. M. & Hunter, R. E. Bedform alignment in directionally varying flows. *Science* **237,** 276–278 (1987).
18. Hay, A. E. & Wilson, D. J. Rotary sidescan images of nearshore bedform evolution during a storm. *Mar. Geol.* **119,** 57–65 (1994).
19. Clifton, H. E. Wave-formed sedimentary structures-a conceptual model. *Beach and Nearshore Sedimentation, SEPM Special Pub.* **24,** 126–148 (1976).
20. Moore, J. N., Fritz, W. J. & Futch, R. S. Occurrence of megaripples in a ridge and runnel system, Sapelo Island, Georgia: morphology and processes. *J. Sedim. Petrol.* **54,** 615–625 (1984).
21. Sherman, D. J., Short, A. D. & Takeda, I. Sediment mixing depth and bedform migration in rip channels. *J. Coastal Res.* **15,** 39–48 (1993).
22. Dalrymple, R. W. & Rhodes, R. N. Estuarine dunes and barforms. *Dev. Sedimentol.* **53,** 359–422 (1995).
23. Hay, A. E. & Bowen, A. J. Alongshore migration of lunate megaripples during DUCK94. *J. Geophys. Res.* (in the press).
24. Gallagher, E. L., Boyd, W., Elgar, S., Guza, R. T. & Woodward, B. Performance of a sonar altimeter in the nearshore. *Mar. Geol.* **133,** 241–248 (1996).
25. Bagnold, R. A. An approach to the sediment transport problem from general physics. *US Geol. Surv. Prof. Paper* **422-I** (1966).
26. Rubin, D. M. Cross-bedding, bedforms, and paleocurrents: Concepts in sedimentology and paleontology. *SEPM Special Pub.* **1** (1987).
27. Fryberger, S. G. Dune forms and wind regime. *A Study of Global Sand Seas, Pap. US Geol. Surv.* **1052,** 137–170 (1979).
28. Rubin, D. M. & Ikeda, H. Flume experiments on the alignment of transverse, oblique, and longitudinal dunes in directionally varying flows. *Sedimentology* **37,** 673–684 (1990).

Acknowledgements. We thank T. Drake for introducing us to ref. 17 and for sharing his insight into, and enthusiasm for, bedforms; R. T. Guza and B. T. Werner for suggestions and advice; D. Rubin for critically reading the manuscript; P. Fields for comments; and R. T. Guza, T. H. C. Herbers and B. Raubenheimer for help with acquiring field data. The instruments were fabricated, deployed and maintained by staff from the Center for Coastal Studies, Scripps Institution of Oceanography; the US Army Corps of Engineers Field Research Facility provided logistical support. Funding was from the Office of Naval Research, the NSF, and the National Research Council.

Correspondence should be addressed to either E.L.G. (email: egallagh@oc.nps.navy.mil) or S.E. (email: elgar@eecs.wsu.edu).

The unique anisotropy of the Pacific upper mantle

Göran Ekström & Adam M. Dziewonski

Department of Earth and Planetary Sciences, Harvard University, 20 Oxford Street, Cambridge, Massachusetts 02138, USA

The development and interpretation of tomographic models of the Earth's mantle have usually proceeded under the assumption that fast and slow seismic velocity anomalies represent a spatially heterogeneous temperature field associated with mantle convection. Implicit in this approach is an assumption that either the effect of anisotropy on seismic velocities is small in comparison with isotropic thermal or compositional effects, or that the tomographic results represent the average isotropic heterogeneity, even if individual seismic observations are affected by anisotropic structure. For example, velocity anomalies in the upper portions of the oceanic mantle are commonly interpreted in terms of the progressive cooling[1,2] (and localized reheating[3]) of a mechanical and thermal boundary layer consisting of rigid oceanic lithosphere and an underlying, less viscous, asthenosphere. Here, however, we present results from a global three-dimensional tomographic model of shear-wave velocity which shows that the uppermost mantle beneath the central Pacific Ocean is considerably more complicated than this simple model. Over a broad area, with its centre near Hawaii, the seismic data reveal a regional anomaly in elastic anisotropy which produces variations of seismic velocities that are at least as large as

those due to thermal effects. Because seismic anisotropy is an indicator of strain in Earth materials, our tomographic results can be used to put constraints on both buoyancy forces (thermal effects) and flow patterns in the upper mantle.

Our finding comes in the context of the development of a high-resolution (up to spherical harmonic degree 20) global, three-dimensional (3D) tomographic model of shear-wave velocity in the Earth's upper mantle. Previously, using a large data set, we obtained an isotropic S-wave velocity model (S20–95; ref. 4) which showed some features different from those seen in the earlier tomographic mantle model S12 (ref. 5). The most striking disagreement between the models occurred at ~150 km depth under the Pacific plate. At this depth, the East Pacific Rise (EPR) is the most pronounced negative (slow) anomaly in model S12, as well as in other recent mantle models[6,7], whereas model S20-95 showed equally slow anomalies in the central Pacific. If model S20-95 were correct, this would have important implications for the controversy surrounding the depth extent of the velocity anomalies at mid-ocean ridges[1,2]. At the same time, the variability of the anomalies shown by different tomographic models at shallow depths beneath the central Pacific would also cast doubt on the robustness of seismic tomographic results in general.

A number of experiments have led us to the conclusion that the difference seen in the Pacific between models S12 and S20-95, and possibly those seen between other tomographic models as well, is largely the result of incompatibility between two groups of data: one consisting of observations with primary sensitivity to V_{SH} (for example, Love waves), the shear-wave velocity of a transversely polarized horizontally travelling S wave, and the other of observations sensitive to V_{SV} (for example, Rayleigh waves), the velocity of a vertically travelling S wave. In an isotropic material, V_{SH} and V_{SV} are equal, but in an anisotropic material they differ. The incorporation or exclusion, or relative weighting, of these different data in an inversion for isotropic S-wave velocity perturbations can lead to undesired compromises in the resulting models. For example, in the derivation of model S12, significantly higher weights were assigned to the V_{SH}-sensitive data, whereas S20-95 was dominated by V_{SV}-sensitive observations. The sensitivity of the results to such weighting schemes indicated to us a need for greater flexibility in the parametrization of the models, and motivated us to look more closely at the possibility of reconciling the different observations by consideration of regional variations in anisotropy.

Most published 3D global models of upper-mantle shear-wave velocity are isotropic, or consist of isotropic perturbations with respect to an anisotropic starting model. There are exceptions; Nataf *et al.*[8,9], for example, proposed global 3D models for V_{SV} and V_{SH}, thus implying spatially variable radial anisotropy (transverse isotropy with a radial symmetry axis). However, these models showed very large (up to 30%) differences in $|V_{SH} - V_{SV}|/V_{SH}$, a finding not supported by later studies. Montagner and Tanimoto[10,11] investigated a more general form of mantle anisotropy, which included azimuthally varying terms, and found larger values for radial anisotropy in the oceanic mantle as compared with the continental mantle. Models derived for specific paths or regions have in several studies included radial anisotropy as an important component[12–16], but often variations in anisotropy have been ignored, reflecting the

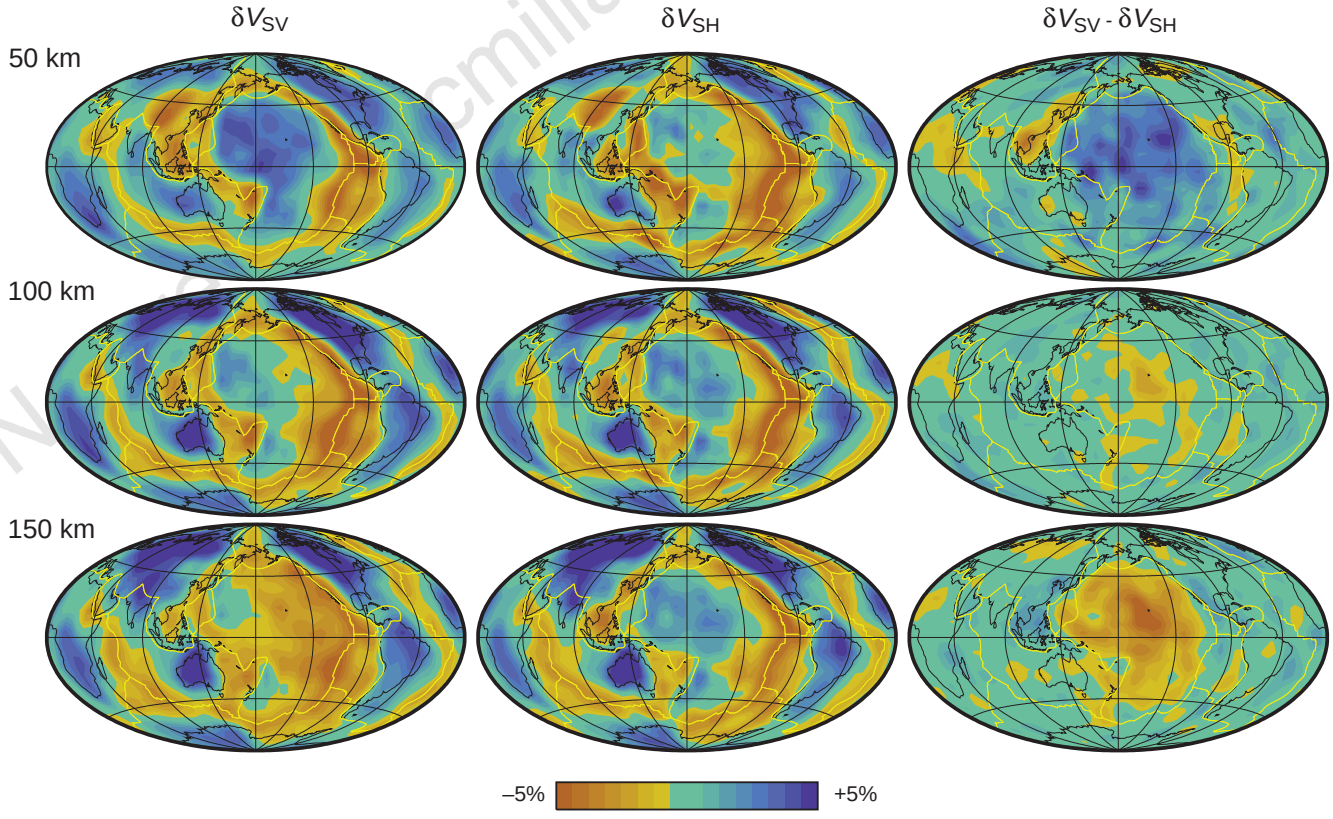

Figure 1 Maps showing the velocity variations in the model S20A at 50, 100, and 150 km depth. The left column shows the lateral variations in V_{SV} with respect to V_{SV}^{PREM}, $\delta V_{SV} = (V_{SV} - V_{SV}^{PREM})/V_{SV}^{PREM}$, the middle column the variations in V_{SH} with respect to V_{SH}^{PREM}, $\delta V_{SH} = (V_{SH} - V_{SH}^{PREM})/V_{SH}^{PREM}$ and the rightmost column the variations in their differences, $(\delta V_{SV} - \delta V_{SH})$. See Fig. 2 for examples of absolute variations in velocity. The top 200 km of the mantle is very well constrained by our data, primarily by the dispersion measurements of intermediate-period Love and Rayleigh waves. The most prominent velocity anomalies in this depth range are associated with the fast mantle roots beneath continental interiors, the slow mid-ocean ridges and back-arc spreading centres, and the fast mantle beneath the oldest sea floor. The data sets used in the derivation of the V_{SH} and V_{SV} heterogeneities in the upper mantle are entirely independent. The similarity between the structures imaged by the two data sets beneath the continents is remarkable, and lends credence to the pronounced differences seen beneath the Pacific plate at 50 and 150 km depth.

assumption that anisotropic effects are small. Nishimura and Forsyth[17,18] studied the variations in anisotropic properties of the Pacific upper mantle in detail—however, their analysis emphasized an age dependence for both isotropic and anisotropic properties. The results presented here suggest that this emphasis may have been too limiting.

Our new model S20A was derived using a wide variety of seismic observations and allowing for anisotropic heterogeneity in the upper mantle (see Methods for details). Figure 1 shows the perturbations in V_{SV} and V_{SH} with respect to their values in the reference model PREM[19] at 50, 100 and 150 km depth in the mantle. At 50 km depth, the V_{SV} and V_{SH} models have very similar patterns of high velocities under the continents and low velocities under the mid-ocean ridges. A pronounced difference between the models is seen beneath the older portions of the Pacific plate. Here, the perturbation in V_{SV} is positive and large, while V_{SH} remains close to the PREM value. In comparison, the difference map for the rest of the world shows minor anomalies not associated with identifiable tectonic elements; such differences, smaller than about ±1%, we consider to represent an unresolved background level.

At 100 km, the differences between the V_{SH} and V_{SV} models are small. The implication is that the radial anisotropy built into PREM, with V_{SH} ~3% faster than V_{SV}, is a good average for both continents and oceans. However, at 150 km depth, the pattern is dramatically different. Whereas V_{SH} shows the central Pacific as faster than the global average, V_{SV} is significantly slower. The anomaly associated with the EPR is much better defined in V_{SH}, where it is clearly centred on the ridge axis; the negative V_{SV} anomalies are instead diffuse, extending to the centre of the Pacific. The maximum difference between the V_{SV} and V_{SH} perturbations of ~5% is obtained for an area just southwest of Hawaii. It is notable that in the global model of Montagner and Tanimoto[11], the largest anisotropic signal seen at this depth lies in the same area, though it has a smaller absolute amplitude. Below 150 km depth, the difference between V_{SH} and V_{SV} beneath the central Pacific becomes smaller (Fig. 2d), and we do not believe we can resolve a difference between the two at depths greater than 250 km with our current data set.

Two main conclusions result from our analysis. First, Fig. 1 shows that for most of the world, the anisotropy of PREM provides a good average. The only large region where this does not hold true is the Pacific plate. Figure 2a, b shows average V_{SV} and V_{SH} values calculated for the mantle beneath the Pacific plate and for the rest of the world. The average anisotropy that we obtain, with V_{SH} ~2–4% faster than V_{SV} between the Moho and 200 km, is similar to that obtained in previous detailed studies of the Pacific upper mantle[13,14,18]. The Pacific plate is large and well sampled by the

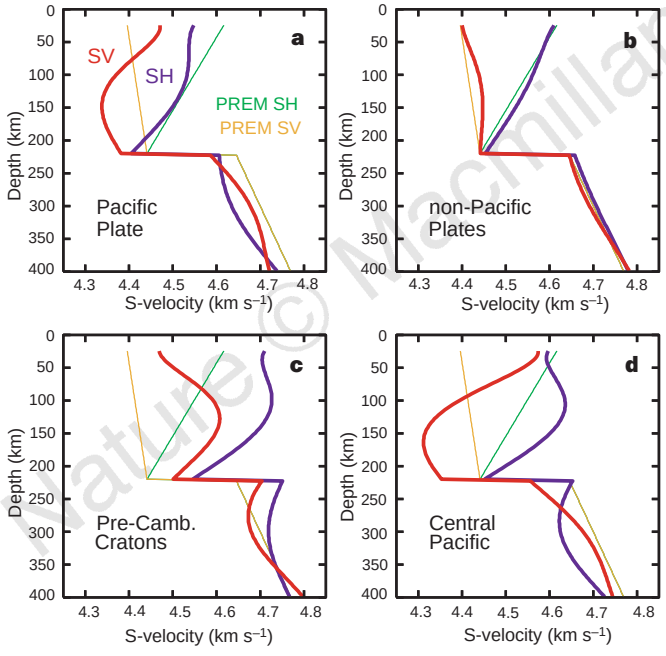

Figure 2 Velocity profiles of the shear-wave velocities V_{SV} and V_{SH}. **a**, The average velocities beneath the entire Pacific plate. The maximum difference between V_{SV} and V_{SH} occurs at around 125 km depth, in contrast to PREM, in which it occurs just below the Moho. Note also that the model shows that the upper mantle beneath the Pacific plate is ~1% slow with respect to PREM down to at least 400 km depth. **b**, The average velocities calculated for all plates except the Pacific. The average structure is close to that of the starting model PREM. **c**, Average velocity profiles calculated for all Precambrian cratons within the Eurasia and North America plates. These regions are sampled very well by our data, and the deviations from the PREM structure are large and well resolved. Note, however, that the difference between V_{SV} and V_{SH} remains very close to that of the starting model PREM. **d**, Average velocity profiles calculated for a cap with 10° radius centred on the anisotropy anomaly identified in this study at 15° N, 160° W. At 130 km depth, V_{SH} is 7% faster than V_{SV}, almost three times the value predicted by PREM. In contrast with PREM, the radial anisotropy in the shallowest mantle is small. Note that the velocity discontinuity at 220 km is part of the starting model PREM, and not a feature that can be resolved in our inversion.

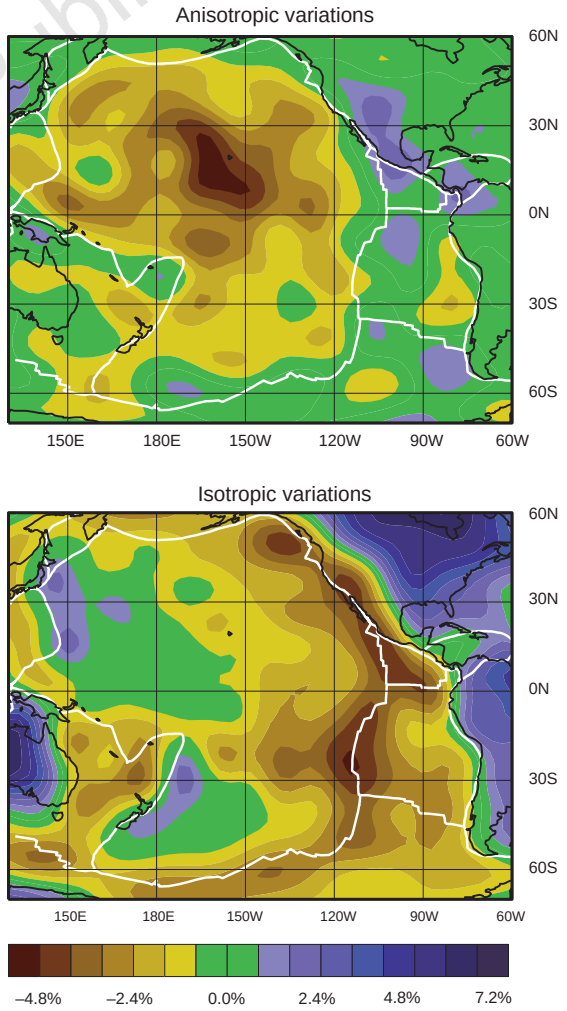

Figure 3 Shear-wave velocity variations beneath the Pacific plate at 150 km depth. The top panel shows the anisotropy $\delta V_{SV} - \delta V_{SH}$ on the same scale as the Voigt-averaged isotropic variation in S-wave velocity (bottom panel) calculated using the approximate expression $\delta V_S^{Voigt} = \frac{1}{3}(\delta V_{SH} + 2\delta V_{SV})$. The maps clearly illustrate that anisotropic velocity variations are as large as the isotropic (thermal) variations. The isotropic S-wave variations correlate better with the age of the ocean floor than either the δV_{SV} or δV_{SH} maps in Fig. 1. The largest deviation from this age correlation is very clearly associated with the location of the Pacific Superswell[3].

data, and we infer that the characteristic anisotropy shown in Fig. 1 is well resolved and unique to the Pacific plate. The North American and Eurasian continents, which are also very well sampled by the data, show very large velocity anomalies with respect to PREM but, surprisingly, very small deviations from the simple anisotropy of PREM (Figs 1 and 2c). The observation that radial anisotropy is required for continental structure agrees with several previous studies[12,15,20,21], though it disagrees with the results of some other workers[22], in particular those of Montagner and Tanimoto[11], who concluded that globally radial anisotropy beneath continents is small.

Our second conclusion is that the geographical variations in radial anisotropy beneath the Pacific plate are large, and do not appear to be correlated with the age of the sea floor (Fig. 3, top map). This large difference between V_{SH} and V_{SV} complicates the interpretation of mapped seismic velocity anomalies[23], as neither V_{SV} nor V_{SH} heterogeneity reflects thermal effects when variations in anisotropy are large. The anisotropic elastic parameters can be combined to form a Voigt average shear modulus[19], which better reflects the isotropic variations in elastic properties—the result of this calculation is shown in Fig. 3. It is striking how well the progression from slow to fast velocities shown in the isotropic average map correlates with the age of the sea floor, with a few notable exceptions: the 'Pacific Superswell'[3] shows velocities which are as slow as those beneath the EPR, and a small, slow anomaly can be seen to the northwest of Hawaii.

The origin of the Pacific anisotropy anomaly shown in Fig. 3 is unknown. Many mantle rocks and minerals show variable and strong anisotropic elastic effects when examined in the laboratory[24]; lattice-preferred orientation (LPO) of olivine due to the shearing of mantle materials during the formation and translation of the plate has been suggested as the main mechanism for generating large-scale seismic anisotropy in both the lithosphere[13,20,25] and the underlying asthenosphere[11,18,26]. However, the generation of radial anisotropy by LPO depends on an azimuthally random, but preferentially horizontal, alignment of olivine crystals. It is unclear what flow and shearing mechanisms exist to accomplish this beneath the middle of the Pacific plate. One possibility is that, in some areas, the shearing in the asthenosphere is not dominated by the coherent plate motions, but instead by processes with characteristic length scales significantly smaller than the resolving length of our model, ~1,500 km. Small-scale convection[27], or a complex pattern of horizontal flow generated by the injection of material into the asthenosphere by mantle plumes, could potentially cause such small-scale variability in the aligning shear motions.

Table 1 Data used in deriving the anisotropic model S20A

Data type	Observations	Sensitivity	Variance reduction
Travel times			
SS-S	5,124	SV	72%
ScS-S	3,543	SV	61%
S-SKS	3,567	SV	55%
SKKS-SKS	2,232	SV	32%
S	26,462	SV	37%
SS	11,417	SV	39%
ScS	4,422	SV	49%
ScSScS	1,230	SV	40%
Long-period waveforms			
Body waves, $T > 45$ s (Z, L)	13,997	SV	28%
Mantle waves, $T > 85$ s (Z, L)	5,523	SV	55%
Mantle waves, $T > 85$ s (T)	2,665	SH	59%
Mantle waves, $T > 135$ s (Z, L)	4,422	SV	40%
Mantle waves, $T > 135$ s (T)	1,710	SH	47%
Mantle waves, $T > 200$ s (Z, L)	4,978	SV	14%
Mantle waves, $T > 200$ s (L)	1,853	SH	23%
Surface wave dispersion			
Rayleigh (R1), 35–150 s	27,948–37,240	SV	68–90%
Love (G1), 35–150 s	15,189–23,947	SH	76–96%
Rayleigh (R1, R2), 150–300 s	18,295–10,256	SV	30–71%
Love (G1, G2), 150–300 s	9,143–3,830	SH	45–73%

See Methods for details of the data shown here.

Although seismic tomography provides a tool for mapping elastic properties of the Earth's interior, it is increasingly clear that the assumptions driving the interpretation of these maps must continue to be questioned. Composition and fabric may, in some regions of the mantle, be as important as thermal effects in generating velocity anomalies. The positive corollary of this complexity is that the estimation of these additional properties may ultimately be of equal importance for inferring the dynamical processes occurring in the deep Earth. □

Methods

Our model parametrization describes 3D S-wave velocity perturbations with respect to PREM[19]. As in earlier studies[28], the model is expanded using basis functions:

$$\delta V_S(r,\theta,\phi)/V_0(r) = \sum_{k=0}^{K}\sum_{l=0}^{L}\sum_{m=0}^{l} f_k(r) \times p_l^m(\cos\theta)({}_kA_l^m \cos m\phi + {}_kB_l^m \sin m\phi) \quad (1)$$

where $V_0(r)$ is the PREM reference velocity, $f_k(r)$ are normalized Chebyshev polynomials, $p_l^m(\cos\theta)$ the associated Legendre polynomials, θ is colatitude, ϕ is longitude, and r is the radius. The upper and lower mantle are described by separate sets of coefficients, and the maximum degree in the radial expansion is $K = 7$ for the upper mantle and $K = 5$ for the lower mantle. In the horizontal direction, the maximum spherical harmonic degree is $L = 20$, for both the upper and lower mantle. (Coefficients describing model S20A are available; see Supplementary Information.)

Table 1 lists the four types of data used in the model inversion. (1) Absolute and differential travel times measured from digital seismograms using a cross-correlation technique[28]. (2) Complete long-period waveforms in several frequency bands. These data are similar to the data used in the early Harvard tomographic models of the upper mantle[29], but the data set has been much expanded. (3) Surface-wave dispersion measurements[30] in the period range 35–150 s. (4) Additional long-period (150–300 s) Love and Rayleigh wave dispersion measurements. The data sets of greatest importance for resolving the anisotropy of the upper mantle are the measurements of Love and Rayleigh wave dispersion, data types (3) and (4).

Five elastic parameters are required to describe a transversely isotropic medium[31]. Using the theory developed by Takeuchi and Saito[32] and Woodhouse and Dziewonski[29], one could attempt an inversion for all five elastic constants, A, C, F, L and N in the notation of Love[31], but our data have only limited independent sensitivity to the first three parameters. Thus, an inversion focused on 3D variations in $V_{SH} = (N/\rho)^{1/2}$ and $V_{SV} = (L/\rho)^{1/2}$ seemed at this stage most practical and straightforward, where ρ is the density. To simplify the calculations, we used average isotropic sensitivity kernels for δV_S calculated for anisotropic PREM in our inversions. We have performed experiments which show that no significant bias is introduced by this approximation (see below). The sensitivity of Rayleigh waves to independent variations in V_{PH} and V_{PV} is not considered in our analysis, but in the calculation of the sensitivity kernels we assume an implicit variation in P-wave velocity such that $\delta V_P/V_P = 0.55\delta V_S/V_S$. Additional experiments using complete anisotropic kernels show that varying the proportionality constant between 0.0 and 1.0 does not significantly affect our results. (Details of these, and the above-mentioned experiments are available; see Supplementary Information.) Because the sensitivity of Rayleigh waves to P-wave velocity is much smaller than that to S-wave velocity, we believe that unrealistically large independent variations in P-wave velocity would be required to influence our main result.

To constrain the V_{SH} and V_{SV} velocities independently in the upper mantle, we divided the data sets into two groups: one with primary sensitivity to V_{SH} and a second with primary sensitivity to V_{SV}. Travel-time data were included in the V_{SV} data set as all measured phases bottom in the lower mantle and have nearly vertical propagation paths in the upper mantle. Rayleigh-wave dispersion and mantle- and body-wave data observed on the vertical and longitudinal components were also included in the V_{SV} data set. Only fundamental-mode Love wave dispersion and mantle-wave data were included in the V_{SH} data set.

The model coefficients (${}_kA_l^m$, ${}_kB_l^m$) were determined by formulating the inverse problem, which minimizes the least-squares misfit between the observed data and corresponding model predictions. The data were inverted

simultaneously for isotropic velocity perturbations in the lower mantle and independent V_{SV} and V_{SH} variations in the upper mantle. Because the true observational and modelling errors are unknown, the different data sets are combined using empirical weighting coefficients based on previous experiments and our subjective judgement. The inversion was damped towards a minimum model and smooth horizontal perturbations. The perturbations were also damped towards continuity across the 670-km discontinuity. No explicit radial damping was imposed in the inversion.

An important step in imaging the shallow mantle is the application of corrections for crustal structure. We correct the Love and Rayleigh wave dispersion curves by subtracting the predicted effect of the crustal model CRUST-5.1 (ref. 33). Travel-time data are also corrected for this crustal model, as well as for topography and bathymetry.

Azimuthal anisotropy, the dependence of velocity on the direction of wave propagation[13,18], is observed to be significant for Rayleigh waves traversing oceanic lithosphere, and could potentially bias our results. We have therefore inverted the Rayleigh wave dispersion data to obtain maps of azimuthal anisotropy, and corrected the data for the azimuthally varying term when inverting for 3D Earth structure. The application of this correction does not, however, materially change the derived 3D models.

The reductions in variance provided by the 3D model S20A with respect to the starting model (PREM) for the various data sets are given in Table 1.

Received 24 July 1997; accepted 6 April 1998.

1. Zhang, Y.-S. & Tanimoto, T. Ridges, hotspots and their interaction as observed in seismic velocity maps. *Nature* **355,** 45–49 (1992).
2. Su, W.-J., Woodward, R. L. & Dziewonski, A. M. Deep origin of mid-ocean-ridge seismic velocity anomalies. *Nature* **359,** 149–152 (1992).
3. McNutt, M. K. & Superswells. *Rev. Geophys. Space Phys.* (in the press).
4. Ekström, G. & Dziewonski, A. M. Improved models of upper mantle S velocity structure. (abstr.) *EOS* **76(46),** F421 (1995).
5. Su, W.-J., Woodward, R. L. & Dziewonski, A. M. Degree-12 model of shear velocity heterogeneity in the mantle. *J. Geophys. Res.* **99,** 4945–4980 (1994).
6. Masters, G., Johnson, S., Laske, G. & Bolton, H. A shear-velocity model of the mantle. *Phil. Trans. R. Soc. Lond. A* **354,** 1385–1411 (1996).
7. Li, X.-D. & Romanowicz, B. Global mantle shear velocity model developed using nonlinear asymptotic coupling theory. *J. Geophys. Res.* **101,** 22245–22272 (1996).
8. Nataf, H. C., Nakanishi, I. & Anderson, D. L. Anisotropy and shear-velocity heterogeneities in the upper mantle. *Geophys. Res. Lett.* **11,** 109–112 (1984).
9. Nataf, H. C., Nakanishi, I. & Anderson, D. L. Measurements of mantle wave velocities and inversion for lateral heterogeneities and anisotropy. *J. Geophys. Res.* **91,** 7261–7307 (1986).
10. Montagner, J.-P. & Tanimoto, T. Global anisotropy in the upper mantle inferred from the regionalization of phase velocities. *J. Geophys. Res.* **95,** 4797–4819 (1990).
11. Montagner, J.-P. & Tanimoto, T. Global upper mantle tomography of seismic velocities and anisotropies. *J. Geophys. Res.* **96,** 20337–20351 (1991).
12. McEvilly, T. V. Central US crust-upper mantle structure from Love and Rayleigh wave phase velocity inversion. *Bull. Seismol. Soc. Am.* **54,** 1997–2015 (1964).
13. Forsyth, D. W. The early structural evolution and anisotropy of the oceanic upper mantle. *Geophys. J. R. Astron. Soc.* **43,** 103–162 (1975).
14. Mitchell, B. J. & Yu, G.-K. Surface wave dispersion, regionalized velocity models, and anisotropy of the Pacific crust and upper mantle. *Geophys. J. R. Astron. Soc.* **63,** 497–514 (1980).
15. Gee, L. S. & Jordan, T. H. Polarization anisotropy and fine-scale structure of the Eurasian upper mantle. *Geophys. Res. Lett.* **15,** 824–827 (1988).
16. Gaherty, J. B., Jordan, T. H. & Gee, L. S. Seismic structure of the upper mantle in a central Pacific corridor. *J. Geophys. Res.* **101,** 22291–22309 (1996).
17. Nishimura, C. E. & Forsyth, D. W. Rayleigh wave phase velocities in the Pacific with implications for azimuthal anisotropy and lateral heterogeneities. *Geophys. J. R. Astron. Soc.* **94,** 479–501 (1988).
18. Nishimura, C. E. & Forsyth, D. W. The anisotropic structure of the upper mantle in the Pacific. *Geophys. J. R. Astron. Soc.* **96,** 203–229 (1989).
19. Dziewonski, A. M. & Anderson, D. L. Preliminary reference Earth model. *Phys. Earth Planet. Inter.* **25,** 297–356 (1981).
20. Lévêque, J. J. & Cara, M. Long-period Love wave overtone data in North America and the Pacific Ocean: new evidence for upper mantle anisotropy. *Phys. Earth Planet. Inter.* **33,** 164–179 (1983).
21. Gaherty, J. B., Kato, M. & Jordan, T. H. Seismological structure of the upper mantle: A regional comparison of seismic layering. *Phys. Earth Planet. Inter.* (submitted).
22. Mitchell, B. J. On the inversion of Love and Rayleigh wave dispersion and implications for earth structure and anisotropy. *Geophys. J. R. Astron. Soc.* **76,** 233–241 (1984).
23. Regan, J. & Anderson, D. L. Anisotropic models of the upper mantle. *Phys. Earth Planet. Inter.* **35,** 227–263 (1984).
24. Birch, F. The velocity of compressional waves in rocks to 10 kilobars. *J. Geophys. Res.* **65,** 1083–1102 (1960).
25. Nicolas, A. & Christensen, N. I. in *Composition, Structure, and Dynamics of Lithosphere-Asthenosphere System* (eds Fuchs, K. & Froidevaux, C.) 111–123 (Geodyn. Ser. Vol. 16, Am. Geophys. Union, Washington DC, 1987).
26. Ribe, N. M. Seismic anisotropy and mantle flow. *J. Geophys. Res.* **94,** 4213–4223 (1989).
27. Parsons, B. & McKenzie, D. Mantle convection and the thermal structure of the plates. *J. Geophys. Res.* **83,** 4485–4496 (1978).
28. Dziewonski, A. M., Ekström, G. & Liu, X.-F. in *Monitoring a Comprehensive Test Ban Treaty* (eds Husebye, E. S. & Dainty, A. M.) 521–550 (Kluwer Academic, Dordrecht, 1996).
29. Woodhouse, J. H. & Dziewonski, A. M. Mapping the upper mantle: Three dimensional modeling of Earth structure by inversion of seismic waveforms. *J. Geophys. Res.* **89,** 5953–5986 (1984).
30. Ekström, G., Tromp, J. & Larson, E. W. F. Measurements and global models of surface wave propagation. *J. Geophys. Res.* **102,** 8317–8157 (1997).
31. Love, A. E. H. *A Treatise on the Theory of Elasticity* 4th edn (Cambridge Univ., 1927).
32. Takeuchi, H. & Saito, M. Seismic surface waves. *Methods Comput. Phys.* **11,** 217–295 (1972).
33. Mooney, W. D., Laske, G. & Masters, G. CRUST-5.1: A global crustal model at 5° × 5°. *J. Geophys. Res.* **103,** 727–747 (1998).

Supplementary information is available on *Nature*'s World-Wide Web site (http://www.nature.com) or as paper copy from the London editorial office of *Nature*.

Acknowledgements. The data used in this work were obtained from the IRIS, GDSN, IDA, GEOSCOPE, MEDNET, CDSN and GTSN seismograph networks. We thank D. Forsyth, J. Gaherty, J. Phipps Morgan, G. Smith and C. Wolfe for discussions, and X.-F. Liu, S. Sianissian and W.-J. Su for help with collecting and preparing the data sets. This work was supported by the US NSF and the US Air Force Office for Scientific Research.

Correspondence and requests for materials should be addressed to G.E. (e-mail: ekstrom@seismology.harvard.edu).

Devonian terrestrial arthropods from Gondwana

Gregory D. Edgecombe

Centre for Evolutionary Research, Australian Museum, 6 College Street, Sydney South, New South Wales 2000, Australia

The origin of the most diverse terrestrial animal group, Atelocerata (myriapods and hexapods), is obscured by an incomplete fossil record[1]. Early (Silurian and Devonian) body fossils of terrestrial arthropods have been found only in Laurussia, with key sites in Britain and eastern North America[2–5]. Although trace fossil assemblages indicate the presence of various arthropods on land in Australia in the Silurian Period[6], definite terrestrial arthropods have not been discovered in mid-Palaeozoic stages of the southern continents. Here I describe the first atelocerates from the Devonian stages of Gondwana; these are perhaps the earliest known remains of Australian land animals. The fossils comprise two closely related myriapod species of the genus *Maldybulakia*, first identified from Kazakhstan[7,8]. They add substantially to our knowledge of the anatomy of this problematic arthropod, and illustrate the widespread distribution of parts of the Devonian terrestrial fauna. A clade including *Maldybulakia* is distinct within the Myriapoda at a high taxonomic level. The existence of *Maldybulakia* and the extinct classes Arthropleuridea and Kampecarida[9], with centipedes and millipedes, indicates the high class-level diversity of myriapods in the Devonian.

The earlier of two new Devonian species of *Maldybulakia* from New South Wales, Australia, is represented by abundant moulds of disarticulated tergites and pleurotergites in sandstones of the Sugarloaf Creek Formation, in the Taemas–Wee Jasper area. These strata are of Early Devonian (latest Lochkovian to earliest Pragian) age, and have a fluvial origin[10]. The second Australian species is found in lacustrine mudstones of the Boyd Volcanic Complex near Eden; these mudstones have been assigned a Late Givetian or Early Frasnian age (ref. 11, and G. C. Young, personal communication). At both sites they are the only animal macrofossils, but the Eden locality has an abundant terrestrial flora. *Maldybulakia* is known from lacustrine facies in the Lower Devonian (Pragian/Emsian) stages of central Kazakhstan[7].

Articulated specimens of *Maldybulakia* (Fig. 1a, b) show the trunk to be composed of two tagmata. The anterior tagma includes one or possibly two trapezoidal tergites. This tergite type is bisected medially by a sinuous, transverse furrow or stricture, and has a sloping anterior section. Although only one of these tergites is found in several articulated specimens of one species, another of the same size is displaced in one specimen, and the considerable variation in this tergite in the other species (Fig. 2a) is suggestive of more than one tergite in this tagma. The posterior trunk tagma is composed of pleurotergites with triangular lateral lobes set off from the posteromedian part of the tergum by deep, diagonal furrows. The anterior part of the tergites is lensoid in outline (Fig. 1e) and is completely overlapped by the preceding pleurotergite in articulation. I accept earlier description of the anterior and posterior parts of these